Observation of knot topology of exceptional points

Wenhui Cao, Weixuan Zhang,* and Xiangdong Zhang

Key Laboratory of Advanced Optoelectronic Quantum Architecture and Measurements of Ministry of Education, Beijing Key Laboratory of Nanophotonics & Ultrafine Optoelectronic Systems, School of Physics, Beijing Institute of Technology, Beijing 100081, China

(Received 15 December 2023; revised 28 March 2024; accepted 29 March 2024; published 15 April 2024)

Exceptional points (EPs), which refer to degeneracies in non-Hermitian systems, have garnered significant attention in the last few years due to their potential applications in the fields of sensing, single-mode lasing, and others. Recently, the complete classification of isolated EPs based on homotopy theory has been proposed, where the topology of energy spectra around EPs can be fully characterized by the braiding group and knot topology. However, there have been few experimental observations of EPs with different knot topologies due to the need for tunable, nonlocal, and nonreciprocal couplings in the proposed non-Hermitian lattice model. Here, we report experimental observation of EPs with different types of knots/links by non-Hermitian electric circuits with voltage-tunable node couplings. Specifically, a second-order EP with trefoil knot topology and a third-order EP with 6_3^3 link topology (according to Rolfsen's table) are achieved. Moreover, we also provide a method on the construction of higher-order Dirac EPs with nested-link topologies, and experimentally construct a sixth-order Dirac EP. Our work provides an artificial platform for exploring EPs with knot and link topologies, offering potential applications in designing EP-based electronic devices.

DOI: 10.1103/PhysRevB.109.165128

I. INTRODUCTION

Non-Hermiticity is prevalent in various branches of physics [1–4] and can give rise to diverse unique phenomena without any Hermitian analogs. The concept of an exceptional point (EP) was initially proposed in the perturbation theory of linear non-Hermitian operators, where eigenvalues and corresponding eigenvectors merge, rendering the non-Hermitian operators defective at the EP [5]. Although EPs were first explored in mathematical physics, subsequent studies have confirmed their existence in classical-wave, cold atom, and quantum systems [6–27]. Previous investigations have unveiled a plethora of intriguing properties at EPs, including unidirectional invisibility [6,7], enhanced sensitivity of higher-order EPs [8,9], and single-mode lasing [10], among others [11–27], offering novel avenues for wave control. Interestingly, it has also been demonstrated that the spectral topology of EPs, such as the Riemann surface surrounding them in two-dimensional (2D) parameter space, can give rise to fascinating phenomena involving mode-switching modulations [28–33]. These modulations have been experimentally observed in various artificial systems like optomechanical structures and coupled optical waveguides [34,35].

On the other hand, the classification of EPs with different spectral topologies has recently attracted significant attention. Previous studies have demonstrated that EPs can be characterized by an integer invariant known as the eigenvalue vorticity [36] or discriminant number [37]. However, this method for classifying EPs still faces several inherent challenges, as EPs with distinct types of spectral topologies may possess the same integer invariant. This difficulty in labeling EPs using an integer invariant, that is suitable for classifying different degenerate points in Hermitian systems, arises from the complex eigenspectra of non-Hermitian systems, where eigenvalues can wind and braid around each other in complex energy space [3,38–46]. In this case, a more comprehensive description of EPs requires additional information on their nearby braiding patterns. Recently, a completely mathematical scheme for classifying EPs has been established using braiding groups and knot topology [47]. It is shown that an nth-order EP (EP_n) in the 2D parameter space can be described by a braid group with n elements, where eigenenergies of the non-Hermitian model are intertwined into a geometric knot along a closed path enclosing EP_n. However, until now there has been a lack of comprehensive experiments directly observing EPs with different spectral knots and links due to requirements for tunable, nonlocal, and nonreciprocal couplings of previously proposed non-Hermitian lattice models. Furthermore, the exploration of constructing non-Hermitian Hamiltonians supporting other exotic EPs, such as higher-order Dirac-type ones [48], through the application of knot topology theories remains unexplored.

In this work, we present the experimental realization of non-Hermitian EPs with diverse knot and link topologies using non-Hermitian electric circuits. By precisely manipulating the voltage-tunable amplitude and phase for node couplings, we have successfully observed an EP_2 exhibiting the trefoil knot topology as well as an EP_3 displaying the 6_3^3 link topology. Furthermore, we have theoretically developed a method to construct higher-order Dirac EPs featuring distinct nested-link topologies and experimentally demonstrated a Dirac EP_6.

*zhangwx@bit.edu.cn

 ©2024 American Physical Society

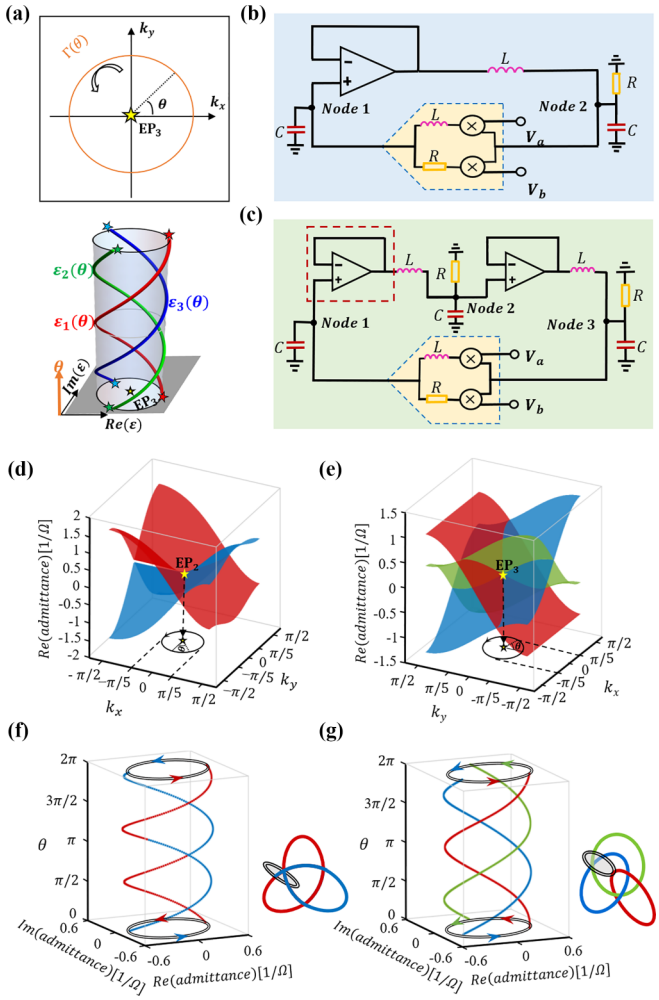

FIG. 1. The theoretical results on the implement of knot topologies of EPs by electric circuits. (a) The illustration of the knot topology related to the braid group B_n for an EP_n. (b), (c) The schematic diagrams of designed electric circuits to fulfill the trefoil knot EP_2 and the 6_3^3 link EP_3, respectively. Red and blue dashed blocks enclose the circuit structures of the voltage follower and the multiplier module. (d), (e) The real parts of eigenspectra for the circuit Laplacian of $L_{(2,3)}$ and $L_{(3,3)}$ in the 2D momentum space. (f), (g) Numerical results of the real part of eigenspectra for $L_{(2,3)}$ and $L_{(3,3)}$ with the 2D k vector (k_x, k_y) evolving along a closed path $\Gamma(\theta)$. Two insets plot 3D structures of energy strands in the form of a trefoil knot and a 6_3^3 link, respectively.

Our work provides an artificial platform for exploring intricate knot/link topologies in EPs and holds tremendous potential in designing highly sensitive electronic sensors.

II. THEORETICAL REALIZATION OF EPs WITH DIFFERENT KNOT AND LINK TOPOLOGIES BY ELECTRIC CIRCUITS

Previous studies have demonstrated that an EP_n in the 2D parameter space can be classified by distinct topological knots and links [47], which exhibit a one-to-one correspondence with conjugacy classes of the braid group B_n. Figure 1(a) illustrates the braiding behavior of three energy bands $[\varepsilon_i(\theta)$, $i = 1$ to 3] along a closed path $\Gamma(\theta)$ parametrized by $k_x = k_0\cos(\theta)$ and $k_y = k_0\sin(\theta)$ ($\theta\in[0, 2\pi]$), enclosing an EP_3 at the center of the 2D k space. It is shown that three energy bands can intertwine in the three-dimensional (3D) parameter space $\{\mathrm{Re}(\varepsilon), \mathrm{Im}(\varepsilon), \theta\}$, and ultimately return to the initial $\mathrm{Re}(\varepsilon)$-$\mathrm{Im}(\varepsilon)$ plane, forming an EP-determined periodic braid. These periodic braids with diverse braiding behaviors can be mapped onto knots or links, thereby revealing the spectral topology associated with EPs. It has been proposed that a non-Hermitian Hamiltonian featuring an EP_p related to a (p, q)-torus knot can be expressed as [47]

$$H_{(p,q)} = \begin{pmatrix} 0 & 0 & 0 & (\sin k_x + i\sin k_y)^q \\ 1 & 0 & 0 & 0 \\ 0 & \ddots & \ddots & 0 \\ 0 & 0 & 1 & 0 \end{pmatrix}_{p\times p}, \quad (1)$$

where there exists a constant nonreciprocal coupling between adjacent sites and a k-dependent nonreciprocal coupling between the end points. It is noted that Eq. (1) can be decomposed into a transposed Jordan block matrix, which possesses a pth-order EP, and a perturbative coupling term that is only dependent on k_x and k_y. Hence, we can tune values of k_x and k_y to construct EPs with $(\sin k_x + i\sin k_y)^q = 0$. In this case, the $\mathrm{EP_p}$ with a (p, q)-torus knot can emerge at momentum points of $(k_x, k_y) = (m\pi, n\pi)$ with $m, n \in 0,\ 1$. It is worth noting that an EP_n with the spectral knot, which is characterized by a single curve formed by all energy bands, should possess a Riemann surface of the eigenspectrum in the 2D parameter space. Conversely, an EP_n with a link topology, where each linked energy circle corresponds to an individual energy band, can exhibit the linear dispersion of the eigenspectrum resembling Dirac EPs (see Appendix A for details). The Dirac EPs and higher-order Dirac EPs refer to second-order and higher-order EPs with linear dispersions around them in (k_x, k_y) space. The linear dispersion around Dirac EPs can be understood analytically. As for the Hamiltonian of Eq. (1), the analytic solutions of its eigenvalues are proportional to the pth complex roots of $(\sin k_x + i\sin k_y)^q$. This indicates that the energy dispersion near the (p, q)-knot EP is proportional to $E \sim |k|^{q/p}$. Therefore, the EP with $p = q$ can exhibit the linear dispersion. In addition, we can also derive the analytical formula for the phase rigidity $r_n = \langle\widetilde{\psi_n^R}|\widetilde{\psi_n^R}\rangle$ ($|\widetilde{\psi_n^R}\rangle$ is the right eigenvector), which is in the form of $r_n \sim \frac{2|k|^q}{|k|^q+1}$ near the $(2, q)$-knot EP (see Appendix B for numerical results). Moreover, the (p, q)-knot EPs also satisfy the non-Hermitian doubling theorem [37,40,49] (see Appendix C).

The experimental realization of the non-Hermitian lattice model described by Eq. (1) in full k space poses a formidable challenge, as it necessitates the incorporation of nonlocal, nonreciprocal, and tunable site couplings between distinct lattice sites. Leveraging the correspondence between circuit Laplacians and lattice Hamiltonians [50–71], electric circuits offer an ideal platform to simulate EP_p with (p, q)-torus knot topologies. In the following, we focus on implementing two models with $(p = 2, q = 3)$ and $(p = 3, q = 3)$, which yield the EP_2 with a trefoil knot and EP_3 with a 6_3^3 link (according to Rolfsen's table [72]). To simulate the braiding among all non-Hermitian energy bands, we design an electric

circuit featuring tunable site couplings that directly realize the Bloch Hamiltonian outlined in Eq. (1) along curve $\Gamma(\theta)$ within 2D k space. Figures 1(b) and 1(c) depict schematic diagrams of designed electric circuits capable of achieving the trefoil knot EP_2 and the 6_3^3 link EP_3, respectively. The constant nonreciprocal coupling between two circuit nodes is achieved by connecting a voltage follower in series with an inductor. The tunable nonreciprocal couplings from node 2 to node 1 in the EP_2 circuit and from node 3 to node 1 in the EP_3 circuit are implemented through a suitably designed module, which comprises two parallel-connected multipliers with an inductor (L) and a resistor (R) acting as loads. By adjusting the external input voltages (V_a and V_b), tunable nonreciprocal coupling can be achieved, where V_a controls the real part of the coupling and V_b controls the imaginary part. Each node is complemented by either a capacitor (C) or a grounded resistor (R) to account for diagonal elements in the circuit Laplacian matrix. Based on Kirchhoff's equation, we can express the circuit Laplacian of two designed electric circuits as

$$L_{(2,3)} = \frac{1}{i\omega L}\begin{bmatrix} -1-i+\omega^2 CL & \frac{V_a}{10}+i\frac{V_b}{10} \\ 1 & -1-\frac{i\omega L}{R}+\omega^2 CL \end{bmatrix}, \tag{2a}$$

$$L_{(3,3)} = \frac{1}{i\omega L}\begin{bmatrix} -1-i+\omega^2 CL & 0 & \frac{V_a}{10}+i\frac{V_b}{10} \\ 1 & -1-\frac{i\omega L}{R}+\omega^2 CL & 0 \\ 0 & 1 & -1-\frac{i\omega L}{R}+\omega^2 CL \end{bmatrix}, \tag{2b}$$

The Laplacians of the designed electric circuits $L_{(2,3)}$ and $L_{(3,3)}$ exhibit identical forms to Hamiltonians $H_{(2,3)}$ and $H_{(3,3)}$ with $\omega^2 = \frac{1}{CL}$ and $R = \omega L$. By adjusting the external input voltages V_a and V_b, the nonlocal coupling term $\frac{V_a}{10} + i\frac{V_b}{10}$ between the first and pth nodes in the designed circuit can achieve $(\sin k_x + i\sin k_y)^q$ with k_x and k_y traversing the path $\Gamma(\theta)$. Notably, the eigenenergy is directly associated with the eigenvalue of the circuit Laplacian. In Appendix D, a detailed derivation of the circuit Laplacian is provided. Herein, we set the circuit parameters as $L = 470$ μH, $R = 100$ Ω, $C = 47$ nF, and $\omega^2 = 1/CL$. In this case, EP_2 and EP_3 can appear at $(k_x, k_y) = (m\pi, n\pi)$ with $m, n \in 0,\ 1$, corresponding to $V_a = V_b = 0$ V.

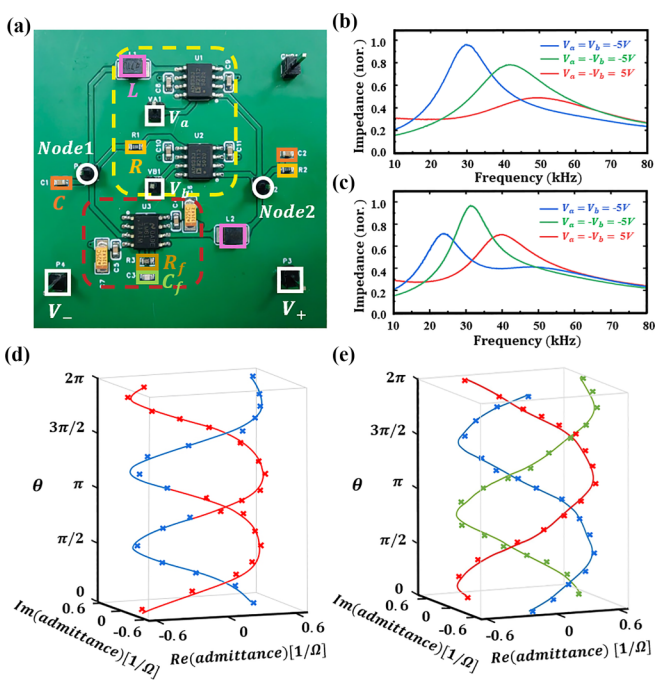

FIG. 2. Experimental results on the observation of trefoil knot and 6_3^3 link topologies for exceptional points in electric circuits. (a) The photograph image of the fabricated circuit sample of $L_{(2,3)}$. (b), (c) The experimental impedance spectra of node 1 with external voltages being ($V_a = V_b = -5$ V), ($V_a = -V_b = -5$ V), between the closing paren and the opening square bracket and ($V_a = -V_b = 5$ V) of the circuit sample with a trefoil knot EP_2 and a 6_3^3 link EP_3. (d), (e) The marker points present the experimentally reconstructed admittance eigenspectra for circuit samples with $L_{(2,3)}$ and $L_{(3,3)}$ along a closed path in the 2D k-vector space. The colored lines plot the simulation results of reconstructed admittance eigenspectra.

Figures 1(d) and 1(e) illustrate the real component of eigenspectra for the circuit Laplacian of $L_{(2,3)}$ and $L_{(3,3)}$, where the EP_2 and EP_3 emerge at the origin of the 2D k space. It is evident that the eigenspectrum surrounding EP_2 (EP_3) exhibits a Riemann surface (a linear dispersion), indicating a knot (link) topology of adjacent admittance bands. To further elucidate knot/link topologies, we compute the real part of eigenspectra for the circuit Laplacian of $L_{(2,3)}$ and $L_{(3,3)}$ at $f = \omega/2\pi = 33.863$ kHz while varying the 2D k vector (k_x, k_y) along a closed path $\Gamma(\theta)$, as depicted in Figs. 1(f) and 1(g). The evolution path $\Gamma(\theta)$ is represented by black lines in Figs. 1(d) and 1(e). It is shown that two (three) strands within the periodic braid are intertwined three times with each other. By connecting top and bottom planes at $\theta = 0$ and 2π, these two periodic braids can transform into a trefoil knot and a 6_3^3 link, as shown in the insets of Figs. 1(f) and 1(g). These findings demonstrate that our designed electric circuit enables the generation of EP_n with different knot and link topologies. Similar to conventional EPs connected by bulk Fermi arcs [4,25], the higher-order (p, q)-knot EPs are also connected by the generalized Fermi arcs defined as the loci in the (k_x, k_y) space when the real parts of any two energy bands have the same value [47].

III. EXPERIMENTAL OBSERVATION OF KNOT TOPOLOGIES OF EPs BY ELECTRIC CIRCUITS

In this section, we fabricate the designed electric circuits to experimentally observe the knot/link topologies of EPs.

Figure 2(a) illustrates a photograph image of the fabricated circuit sample with $L_{(2,3)}$ (the image related to $L_{(3,3)}$ can be found in Appendix E). Two nodes labeled by white circles correspond to node 1 and node 2. The power supply interfaces for the active devices are denoted as V_+ and V_-. The voltage follower module enclosed by the red square employs an LM6171 OpAmp provided by Texas Instruments. To ensure stability, the resistor R_f and capacitor C_f are connected in parallel between the reverse input and output of the OpAmp, while inductor L is connected to its output. The analog-multiplier module framed by the yellow square consists of two AD633 analog multipliers from Analog Devices Inc., which have transfer functions $U_i = \frac{(X_i - X_i')(Y_i - Y_i')}{10\ \mathrm{V}} + Z$ with $i = 1$ or 2. One output from each of these analog multipliers is connected to inductor L, while the other is connected to resistor R. External voltages V_a and V_b are applied via two pins to adjust the coupling term through voltage input. Filter capacitors at OpAmp power supply pins effectively filter ac noise and high-frequency interference signals, providing a stable dc operating voltage. It should be noted that circuit element tolerance is limited within only 1% to prevent detuning of circuit responses. Furthermore, circuit parameters including $L = 470\ \mu\mathrm{H}$, $R = 100\ \Omega$, $C = 47$ nF, $R_f = 2\ \mathrm{k}\Omega$, and $C_f = 100$ pF are set to be sufficiently large, making the influence of effective resistances and parasitic capacitances in the circuit sample negligible. Details on the sample fabrication are provided in Appendix F. To ensure the tunability of two circuit samples, we measure the impedance spectra of node 1 with external voltages being ($V_a = V_b = -5$ V), ($V_a = -V_b = -5$ V), and ($V_a = -V_b = 5$ V), corresponding to the cases with $(k_x, k_y) = (0.217\pi, -0.217\pi)$, $(0.217\pi, 0.217\pi)$, and $(0.33\pi, -0.074\pi)$, as shown by blue, green, and red lines in Figs. 2(b) and 2(c). These measurements possess a good consistency with simulation results, as detailed in Appendix G, indicating the effectiveness of the two samples.

To further explore different knot/link topologies related to the trefoil knot EP_2 and 6_3^3 link EP_3, we experimentally reconstruct admittance band structures for both electric circuits by measuring global voltage responses across all circuit nodes under ac voltage excitation into each node. Details on this experimental measurement can be found in Appendix H. The discretized points in Fig. 2(d) present the experimentally reconstructed admittance eigenspectrum for the circuit sample with $L_{(2,3)}$ along a closed path in the 2D k-vector space [the same path as that plotted in Fig. 1(d)]. The colored lines correspond to associated simulation results. It is clearly shown that the experimentally reconstructed admittance eigenspectrum has good consistency with the simulation, where the two-strand braid with a three-times twisting is obtained. By applying periodic boundary conditions on top ($\theta = 2\pi$) and bottom ($\theta = 0$) planes, a trefoil knot around EP_2 can be obtained, as shown in the inset of Fig. 2(d). Then we examine the circuit sample of $L_{(3,3)}$. The experimentally reconstructed admittance eigenspectrum along the identical path as that used in the circuit sample of $L_{(2,3)}$ is depicted in Fig. 2(e) using discretized points, while the lines represent simulation results. It is shown that the reconstructed admittance eigenspectrum exhibits a three-strand braid twisted thrice, exhibiting excellent agreement with the theoretical prediction. These findings unequivocally demonstrate the experimental realization of exotic knot and link topologies for EP_2 and EP_3. It is worth noting that our experimental approach can also be utilized to study the splitting behavior passing through the EP. In Appendix I, we conduct numerical calculations and experimental measurements on the splitting behaviors of eigenspectra passing through the trefoil knot EP_2 and 6_3^3 link EP_3. It can be observed that the trefoil knot EP_2 exhibits a nonlinear splitting *in the form of* $E \sim |k|^{3/2}$, and the EP_3 with 6_3^3 link topology displays the linear splitting behavior of $E \sim |k|$, being consistent with the properties of Dirac EPs.

IV. DIRAC EP WITH THE NESTED-LINK TOPOLOGY

Beyond the (p, q)-torus knot EPs, in the following, we present a general approach to construct higher-order Dirac EPs using the nested-link topology. It is worth mentioning that the nested link can be represented as a hierarchically periodic braid [73], which is merely a subset of the braid group. Figure 3(a) illustrates an example of a hierarchically periodic braid with each generation possessing a cross section of radius r_n. The green and red lines represent first- and second-generation braids respectively, while orange and blue lines indicate $(n-1)$th-generation and nth-generation braids. Here, the first-generation braid is composed of three effective strands, while subsequent generations consist of two effective strands. In this case, each strand in the first-generation braid comprises two second-generation braids, and each second-generation braid contains two third-generation braids. By iteratively repeating this process, we can construct a generalized nested braid structure exhibiting fractal-like geometry. Finally, merging two end planes results in achieving the nested link.

To incorporate the nested link into the EP spectrum in the 2D k space, we align the transverse plane of the nested braid with the (k_x, k_y) plane. It is important to note that our focus lies on nested braids having an equal number of effective strands and the twisting time within the same generation. In this scenario, an effective strand in the ith-generation braid can be denoted as $S_{\boldsymbol{M}_i}$, where vector $\mathbf{M}_i = (m_1, m_2, \ldots, m_i)$ signifies its generational sequence with m_l ($l = 1$ to i) representing the m_l-th effective strand in the lth-generation braid. Consequently, we can describe the position of effective strand $S_{\boldsymbol{M}_i}$ in the (k_x, k_y, θ) space as

$$k_x(\mathbf{M}_i) = \sum_{\updownarrow=1}^{i} k_{\updownarrow} \cos(w_{\boldsymbol{m}_{\updownarrow}}\theta + \varphi_{\boldsymbol{m}_{\updownarrow}}),\ k_y(\mathbf{M}_i) = \sum_{\updownarrow=1}^{i} k_{\updownarrow} \sin(w_{\boldsymbol{m}_{\updownarrow}}\theta + \varphi_{\boldsymbol{m}_{\updownarrow}}), \tag{3}$$

where $\varphi_{\boldsymbol{m}_{\updownarrow}}$ and $w_{\boldsymbol{m}_{\updownarrow}}$ represent the initial rotation angle and the twisting number of the m_l-th effective strand in the lth-generation braid. $k_{\updownarrow}$ is the radius of the lth-generation braid, and θ is the azimuthal angle of a closed curve in k space.

Next, we establish a correspondence between such a nested braid in k space and the eigenspectrum of a non-

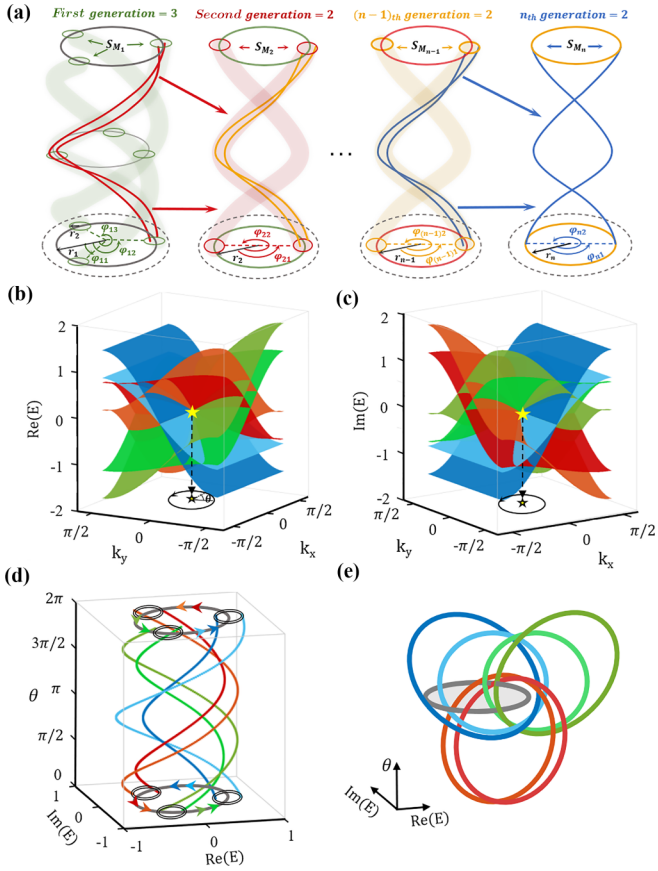

FIG. 3. The theory on the construction of EPs with nested knot topology. (a) The illustration of the hierarchically periodic braid with three generations. The bottom inset presents an enlarged view of the starting plane of the nested braid. (b), (c) Numerical results of the real and imaginary parts of eigenspectra for the non-Hermitian Hamiltonian sustaining a sixth-order EP with a two-generation nested knot in the 2D k space. (d) Numerical results on the real part of eigenenergies with the evolution of (k_x, k_y) along a closed path $\Gamma(\theta)$. (e) The illustration of the nested knot of eigenenergies around the sixth-order EP.

Hermitian Hamiltonian near an EP. It is well established that the energy-knot/link encircling an EP can be interpreted as the roots (or nodal set) of the characteristic polynomial associated with the k-space non-Hermitian Hamiltonian along a closed trajectory in momentum space. In this this, we can mathematically express the requisite characteristic polynomial as

$$q(\varepsilon, k_x, k_y) = \prod_{m_1=1}^{n_1}\prod_{m_2=1}^{n_2}\cdots\prod_{m_i=1}^{n_i}\{\varepsilon - [k_x(\mathbf{M}_i) + ik_y(\mathbf{M}_i)]\}$$
$$= \prod_{m_1=1}^{n_1}\prod_{m_2=1}^{n_2}\cdots\prod_{m_i=1}^{n_i}\left\{\varepsilon - \sum_{\updownarrow=1}^{i} k_{\updownarrow}(k_x + ik_y)^{w_{m_{\updownarrow}}} \times \exp\left(i\varphi_{\boldsymbol{m}_{\updownarrow}}\right)\right\}. \quad (4)$$

To obtain the non-Hermitian Hamiltonian with a nested-link EP, the characteristic polynomial should be expanded in the series of ε as $q(\varepsilon, k_x, k_y) = \varepsilon^N - \sum_{j=0}^{N-1} t_j(k_x, k_y)\varepsilon^j$ with $N = n_1 n_2 \ldots n_i$. The non-Hermitian Hamiltonian possessing an EP_N with a nested link is written as

$$H_N = \begin{pmatrix} t_{N-1}(k_x, k_y) & \cdots & \cdots & t_0(k_x, k_y) \\ 1 & 0 & 0 & 0 \\ 0 & \ddots & \ddots & 0 \\ 0 & 0 & 1 & 0 \end{pmatrix}_{N\times N}. \quad (5)$$

It is important to note that the Hamiltonian H_N is reduced to a N by N Jordan block at $(k_x = 0, k_y = 0)$ with $t_i(k_x, k_y) = 0$ ($i = 1$ to N–1). In this case, an EP_N with the nested-link topology can appear at the origin of 2D k space.

To validate the accuracy of our proposed non-Hermitian Hamiltonian, we investigate a specific non-Hermitian lattice model that supports a Dirac EP_6 with the nested-link topology. Here, we consider a nested braid with two generations, where the corresponding parameters are $k_1 = 1.1$, $k_2 = 0.3$, and $w_{\mathbf{M}_i} = 1$. Figures 3(b) and 3(c) illustrate the real and imaginary parts of eigenspectra for this model in the 2D k space. It is evident that a Dirac EP_6 emerges at $(k_x, k_y) = (0, 0)$ exhibiting the linear dispersion, wherein the real and imaginary parts of all six energy bands coincide. To further elucidate the nested-link topology associated with the Dirac EP_6, we calculate the real part of eigenenergies while varying (k_x, k_y) along a closed path $\Gamma(\theta)$, as depicted in Fig. 3(d). It is shown that a nested braid with two generations can be achieved. By merging the top and bottom planes of this nested braid, we obtain a nested-link configuration, as shown in Fig. 3(e). These results unequivocally demonstrate both the validity and efficiency of our method in designing EP_n featuring nested-link topologies. More examples of higher-order EPs with nested knot/link topologies are applied in Appendix J.

V. OBSERVATION OF DIRAC EP_6 WITH THE NESTED-LINK TOPOLOGY BY ELECTRIC CIRCUITS

To achieve a Dirac EP_6 with the nested-link topology, we design an electric circuit with six nodes, as shown in Fig. 4(a). The voltage follower module enables a constant nonreciprocal coupling between adjacent nodes, while the multiplier module facilitates tunable complex couplings through two external input voltages within each module (denoted as $V_{a,n}$ and $V_{b,n}$ with $n = 1, \ldots, 6$). It is important to note that unlike the circuit design in Fig. 1, capacitors C and C_a are used instead of inductors in both the voltage follower module and multiplier module to ensure stability. Moreover, to achieve the tunable matrix element $H_6(1, 1)$, a combined module consisting of a multiplier module and a voltage follower is employed with grounding at node 1. The inductor L_g is grounded at node 1, while resistors R_g are grounded at the other nodes. We

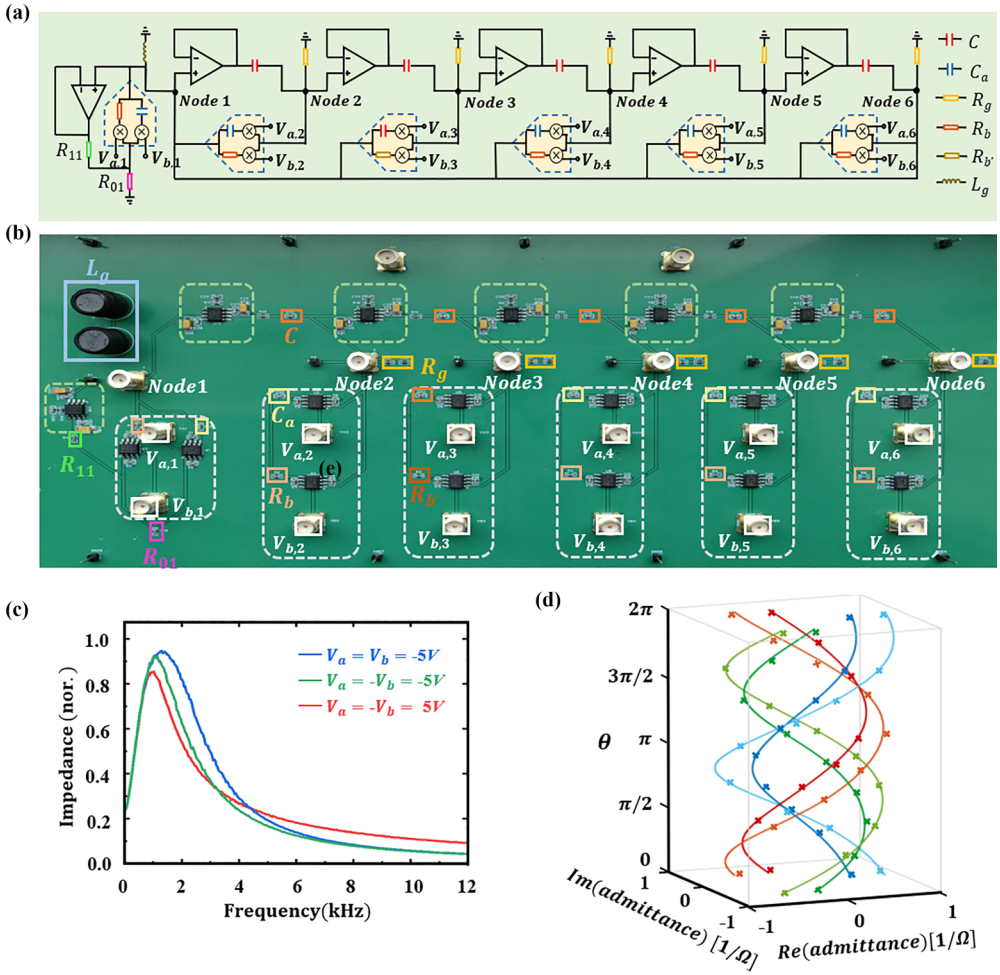

FIG. 4. Experimental results on the observation of the nested link for a sixth-order Dirac EP in electric circuits. (a) The schematic diagram of the designed electric circuit for the realization of a nested knot related to the sixth-order exceptional point. (b) The photograph image of the fabricated electric circuits. (c) The measured impedance spectra of node 1 with the external voltages being ($V_a = V_b = -5$ V), ($V_a = -V_b = -5$ V), and ($V_a = -V_b = 5$ V). (d) Experimental results of the real part of the recovered eigenspectrum, which is in the form of a nested periodic braid, along a closed line in the 2D k-vector space for the circuit sample.

can express the circuit Laplacian as

$$L_6 = i\omega C \begin{bmatrix} a_1 + ib_1 & a_2 + ib_2 & a_3 + ib_3 & a_4 + ib_4 & a_5 + ib_5 & a_6 + ib_6 \\ 1 & D & 0 & 0 & 0 & 0 \\ 0 & 1 & D & 0 & 0 & 0 \\ 0 & 0 & 1 & D & 0 & 0 \\ 0 & 0 & 0 & 1 & D & 0 \\ 0 & 0 & 0 & 0 & 1 & D \end{bmatrix}, \tag{6}$$

with $D = -(1 + \frac{1}{\omega^2 L_g C} - \frac{1}{\omega C R_g})$, $a_1 + ib_1 = 1.5i - 1.5 + \frac{R_{11}}{R_{11}+R_{01}}(-\frac{V_{a,1}}{100} + i\frac{V_{b,1}}{100})$, $a_3 + ib_3 = -\frac{V_{a,3}}{10} + i\frac{V_{b,3}}{10}$, and $a_n + ib_n = -\frac{V_{a,n}}{100} + i\frac{V_{b,n}}{100}$ ($n = 2, 4, 5, 6$). It is clearly shown that the circuit Laplacian possesses a form identical to the non-Hermitian Hamiltonian with a nested-link EP under $R_g = \frac{2}{3\omega C}$ and $L_g = \frac{2}{\omega^2}C$. The detailed derivation of the circuit Laplacian is provided in Appendix K.

The photograph image of the fabricated circuit sample is shown in Fig. 4(b). Here, the circuit parameters are set as $C_a = 10$ nF, $R_b = 10$ kΩ, $C = 100$ nF, $R_{b'} = 1$ kΩ, $R_g = 666$ Ω, $R_{11} = 100$ Ω, $R_{01} = 100$ kΩ, and $L_g = 200$ mH. The measured impedance spectra of node 1 under the external voltages being ($V_a = V_b = -5$ V), ($V_a = -V_b = -5$ V), and ($V_a = -V_b = 5$ V) (matching the simulation results in Appendix E) are displayed in Fig. 4(c). Furthermore, Fig. 4(d) presents the real part of experimentally recovered admittance eigenspectra at $f = \omega/2\pi = 1.591$ kHz along a closed curve $\Gamma(\theta)$ in the 2D k space. It is clearly shown that six energy strands can form a nested braid with two generations. By imposing periodic boundary conditions on the top and bottom

planes, a nested energy link related to the Dirac EP_6 can be constructed, as shown in Fig. 3(e). Furthermore, the numerical and experimental results on the splitting behavior of eigenspectra passing through the nested-link EP_6 are presented in Appendix I. The linear dispersion passing through the EP_6 satisfies the properties of Dirac EPs.

VI. CONCLUSION

In conclusion, we have theoretically designed and experimentally demonstrated the realization of EPs with different knot/link topologies by non-Hermitian electric circuits. Both an EP_2 with the trefoil knot topology and an EP_3 with the 6_3^3 link topology have been observed. Moreover, a method for the construction of non-Hermitian lattice models with different types of nested energy links of EPs has been provided, and a Dirac EP_6 has been observed by electric circuits. Our findings suggest a useful platform to engineer complicated knot topology of higher-order EPs, and may have potential applications in the field of designing electronic sensors with different knot topologies.

ACKNOWLEDGMENTS

This work is supported by the National Key R & D Program of China under Grant No. 2022YFA1404900, Young Elite Scientists Sponsorship Program by CAST Grant No. 2023QNRC001, Beijing Natural Science Foundation Grant No. 1242027 and National Science Foundation of China Grant No. 12104041.

APPENDIX A: NUMERICAL RESULTS OF EIGENSPECTRA WITH DIFFERENT KNOT AND LINK TOPOLOGIES AROUND EPs

In this appendix, we present numerical results of eigenspectra with different (p, q)-torus knots and links around EPs. Figures 5(a)–5(c) plot the eigenspectra of $H_{(p,q)}$ with $(p = 2, q = 1)$, $(p = 2, q = 3)$, and $(p = 2, q = 5)$, respectively. The bottom insets display results of the real part of eigenspectra with the 2D k vector (k_x, k_y) evolving along a closed path, and the associated 3D knotted energy strands are also plotted. It is clearly shown that energy knots can embedded into Riemann surfaces with different geometries, that manifest the topology of knotted EPs. Moreover, we also calculate the eigenspectra of $H_{(p,q)}$ with $(p = 2, q = 2)$, $(p = 3, q = 2)$, and $(p = 4, q = 2)$, as shown in Figs. 5(d)–5(f). Three insets present the evolution of the real part of eigenspectra along a closed curve in the 2D k space and the linked energy strands. We find that the second, third, and fourth Dirac EPs appear at the origin, and different types of energy links exist around the Dirac EPs.

APPENDIX B: NUMERICAL RESULTS AND DISCUSSIONS ON ENERGY DISPERSIONS AND PHASE RIGIDITIES AROUND EPs WITH DIFFERENT VALUES OF *p* AND *q*

In this appendix, we present numerical results and discussions on energy dispersions and behaviors of phase rigidities around EPs with different values of p and q. Firstly, we plot the calculated results on the splitting behavior of the real part of eigenspectra passing through the trefoil knot EP_2 ($p = 2$ and $q = 3$) along the $k_y = 0$ path, as shown in Fig. 6(a). It can be observed that the trefoil knot EP_2 exhibits a nonlinear dispersion on the form of $E \sim |k|^{3/2}$. For comparison, the energy spectra through EP_2 with $(p = 2, q = 2)$ and $(p = 2, q = 1)$ are further presented in Figs. 6(b) and 6(c), where the linear dispersion $E \sim |k|$ and the square-root dispersion $E \sim |k|^{1/2}$ are observed, respectively.

Then we study the behavior of eigenvectors close to EPs with different values of p and q. We can also derive the analytical formula for the phase rigidity $r_n = \langle \widetilde{\psi_n^R} | \widetilde{\psi_n^R} > (|\widetilde{\psi_n^R}\rangle$ is the right eigenvector), which is in the form of $r_n \sim \frac{2|k|^q}{|k|^q+1}$ near the $(2, q)$-knot EP. To further illustrate this relation, we calculate the phase rigidities of the model with $(p = 2, q = 3)$, $(p = 2, q = 2)$, and $(p = 2, q = 1)$ along the path of $k_y = 0$, as displayed in Figs. 6(d)–6(f). It is shown that numerical results are consistent with our analytical formula close to $(2, q)$-knot EPs.

APPENDIX C: NON-HERMITIAN DOUBLING THEOREM OF DIRAC EPS

In this appendix, we illustrate that the EPs considered in our work satisfy the non-Hermitian doubling theorem, where EPs are not presented individually. To illustrate this effect, we add a perturbative coupling term into $H_{(3,3)}$, and the total Hamiltonian becomes

$$H = H_{(3,3)} + m\begin{pmatrix} 0 & 0 & 1 \\ 0 & 0 & 0 \\ 0 & 0 & 0 \end{pmatrix},$$

where the second term represents the perturbation term, and $H_{(3,3)}$ is the Hamiltonian with the 6_3^3 link EP_3 considered in our paper. To illustrate the evolution of EPs in the (k_x, k_y) space, Fig. 7 plots the positions of EPs with the parameter m being changed from 0 to -1. It is shown that $H_{(3,3)}$ with $m = 0$ exhibiting four EP_3 with $(k_x, k_y) = (0, 0)$, $(0, \pi)$, $(\pi, 0)$, (π, π). By decreasing m to -0.5, two pairs of EPs approach each other. When $m = -1$, two EPs simultaneously disappear. In this process, it is indicated that EPs disappear or appear in pairs, satisfying that the sum of the discriminant numbers of all EPs is zero.

In our calculations and measurements, we only focus on a narrow range in the two-parameter space around $(k_x, k_y) = (0, 0)$, where only one pth-order EP exists.

APPENDIX D: DETAILED DERIVATION OF CIRCUIT LAPLACIAN SUSTAINING EPs WITH THE TREFOIL KNOT AND THE 6_3^3 LINK TOPOLOGIES

In this appendix, we provide a detailed derivation of the circuit Laplacian for our designed electric circuits. Firstly, we consider the circuit with the trefoil knot EP. Carrying out the Kirchhoff's law on two circuit nodes, we get the following equations as

$$I_1 = I_L + I_R + I_c, \tag{D1a}$$

$$I_2 = I_L + I_c + I_R, \tag{D1b}$$

where the right-hand side of the equations represent the sum of the currents flowing into the circuit nodes. It is noted

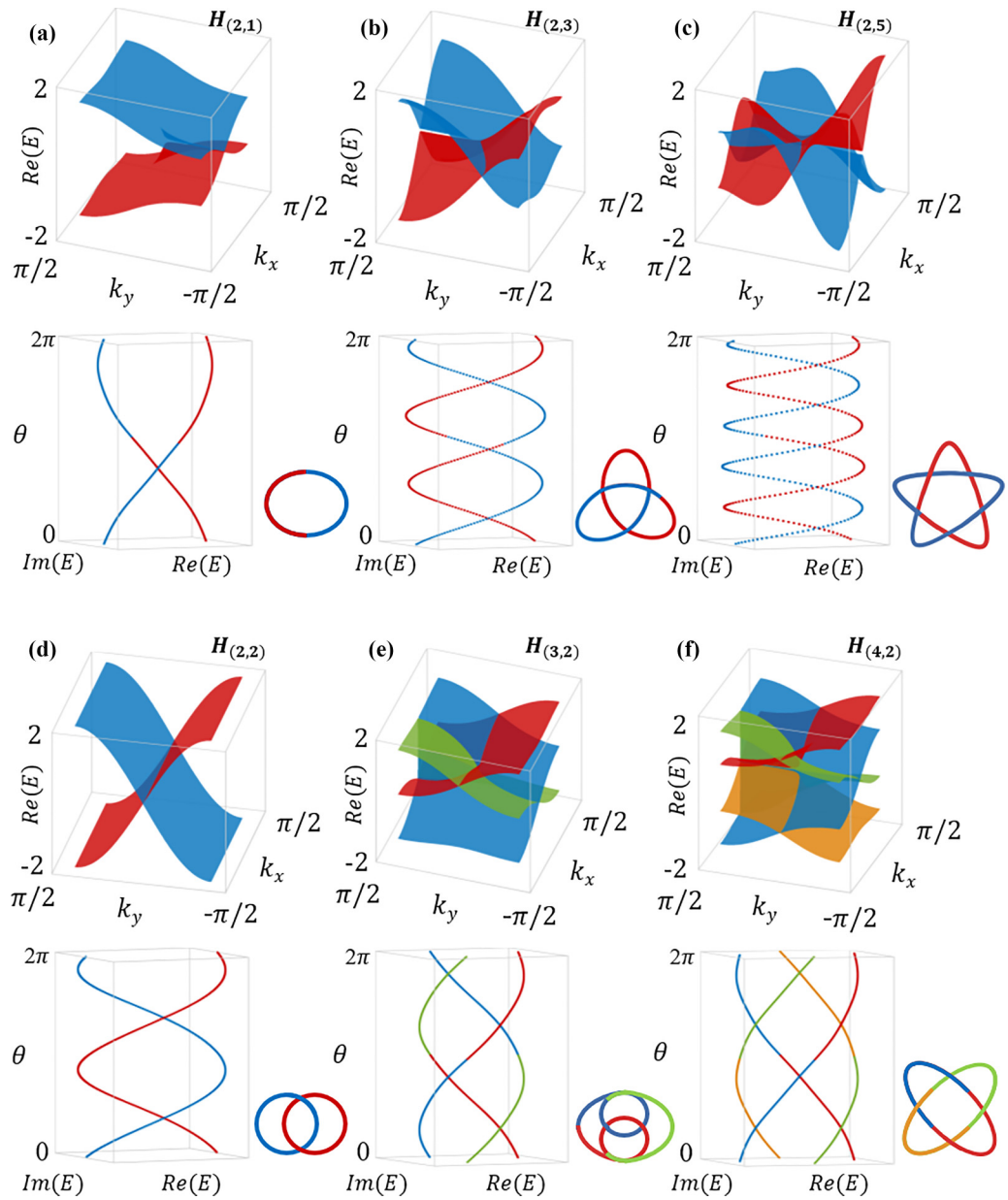

FIG. 5. Numerical results of eigenspectra with different knot and link topologies around EPs. (a)–(c) The eigenspectra of $H_{(p,q)}$ with ($p = 2, q = 1$), ($p = 2, q = 3$), and ($p = 2, q = 5$). (d)–(f) The eigenspectra of $H_{(p,q)}$ with ($p = 2$, q = 2), ($p = 3, q = 2$), and ($p = 4, q = 2$). Insets display the real part of eigenspectra along a closed path in the 2D k space, and the associated 3D knotted energy strands.

that no current is flowing into any of the inputs for the multipliers and the OpAmps. Using the transfer function of the multipliers, we can obtain the detailed expression of Eq. (D1) as

$$I_1 = \left(\frac{aV_2}{i\omega L} - \frac{V_1}{i\omega L}\right) + \left(\frac{bV_2}{R} - \frac{V_1}{R}\right) - \frac{V_1}{i\omega C}, \quad \text{(D2a)}$$

$$I_2 = \frac{1}{i\omega L}(V_1 - V_2) - \left(\frac{1}{R} + \frac{1}{i\omega C}\right)V_2, \quad \text{(D2b)}$$

with $a = \frac{V_a}{10V}$ and $b = \frac{V_b}{10V}$. Choosing $R = \omega L$, Eq. (D2) can be written in the matrix form as

$$\begin{pmatrix} I_1 \\ I_2 \end{pmatrix} = \frac{1}{i\omega L}\begin{pmatrix} -1 - i + \omega^2 CL & a + ib \\ 1 & -1 - \frac{i\omega L}{R} + \omega^2 CL \end{pmatrix}\begin{pmatrix} V_1 \\ V_2 \end{pmatrix}. \quad \text{(D3)}$$

It is shown that the real part of the diagonal elements can be set to zero by setting $\omega^2 = \frac{1}{CL}$. The remaining imaginary part on the diagonal only induces a constant shift and the eigenspectra structure is not affected. We note that Eq. (D3) possesses the same form with the

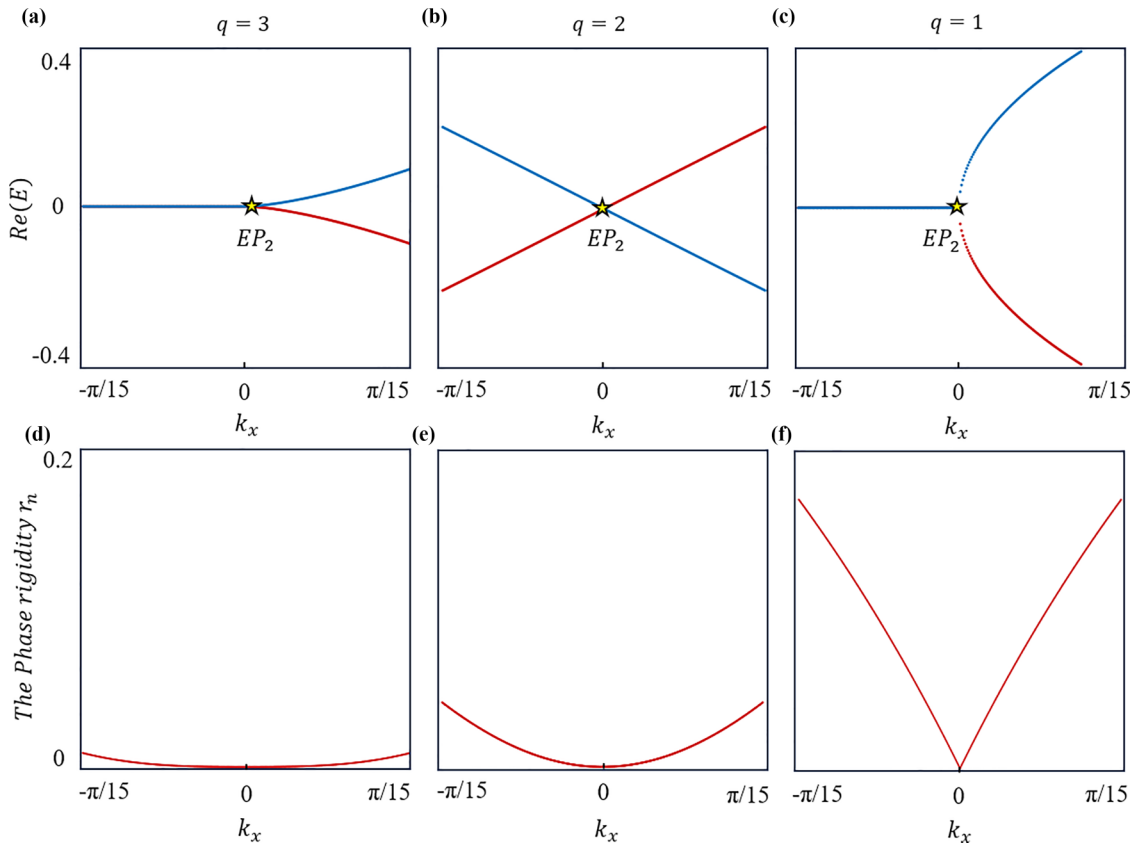

FIG. 6. Numerical results of energy dispersions and phase rigidities around (2, q)-knot EP. (a)–(c) The energy dispersions around EPs with ($p = 2$, $q = 3$), ($p = 2$, $q = 2$), and ($p = 2$, $q = 1$). (d)–(f) The phase rigidities around EPs with ($p = 2$, $q = 3$), ($p = 2$, $q = 2$), and ($p = 2$, $q = 1$).

Hamiltonian matrix of $H_{(2,3)}$, where the k-dependent effective tight-binding parameters $(\sin k_x + i\sin k_y)^3$ can be realized by tuning external voltages of V_a and V_b to make the equation $a + bi = (\sin k_x + i\sin k_y)^3$ satisfied at different k vectors.

Additionally, we consider the 6_3^3 link circuit. Carrying out the Kirchhoff's law on three circuit nodes, we get the following equations as

$$I_1 = I_L + I_R + I_c, \tag{D4a}$$

$$I_2 = I_L + I_c + I_R, \tag{D4b}$$

$$I_3 = I_L + I_c + I_R, \tag{D4c}$$

where the right-hand sides of the equations represent the sum of the currents flowing into the circuit nodes. Using the transfer function of the multipliers, we can obtain the detailed expression of Eq. (D4) as

$$I_1 = \left(\frac{aV_2}{i\omega L} - \frac{V_1}{i\omega L}\right) + \left(\frac{bV_2}{R} - \frac{V_1}{R}\right) - \frac{V_1}{i\omega C}, \tag{D5a}$$

$$I_2 = \frac{1}{i\omega L}(V_1 - V_2) - \left(\frac{1}{R} + \frac{1}{i\omega C}\right)V_2, \tag{D5b}$$

$$I_3 = \frac{1}{i\omega L}(V_2 - V_3) - \left(\frac{1}{R} + \frac{1}{i\omega C}\right)V_3, \tag{D5c}$$

with $a = \frac{V_a}{10V}$ and $b = \frac{V_b}{10V}$. Choosing $R = \omega L$, Eq. (D5) can be written in the matrix form as

$$\begin{pmatrix} I_1 \\ I_2 \\ I_3 \end{pmatrix} = \frac{1}{i\omega L}\begin{pmatrix} -1 - i + \omega^2 CL & 0 & a + ib \\ 1 & -1 - \frac{i\omega L}{R} + \omega^2 CL & 0 \\ 0 & 1 & -1 - \frac{i\omega L}{R} + \omega^2 CL \end{pmatrix}\begin{pmatrix} V_1 \\ V_2 \\ V_3 \end{pmatrix}. \tag{D6}$$

Similar to Eq. (D3), it is shown that the real part of the diagonal elements can be set to zero by setting $\omega^2 = \frac{1}{CL}$. We note that Eq. (D6) possesses the same form with the Hamiltonian matrix of $H_{(3,3)}$, where the k-dependent effective tight-binding parameters $(\sin k_x + i\sin k_y)^3$ can be realized by tuning external voltages of V_a and V_b to make the equation $a + bi = (\sin k_x + i\sin k_y)^3$ satisfied at different k vectors.

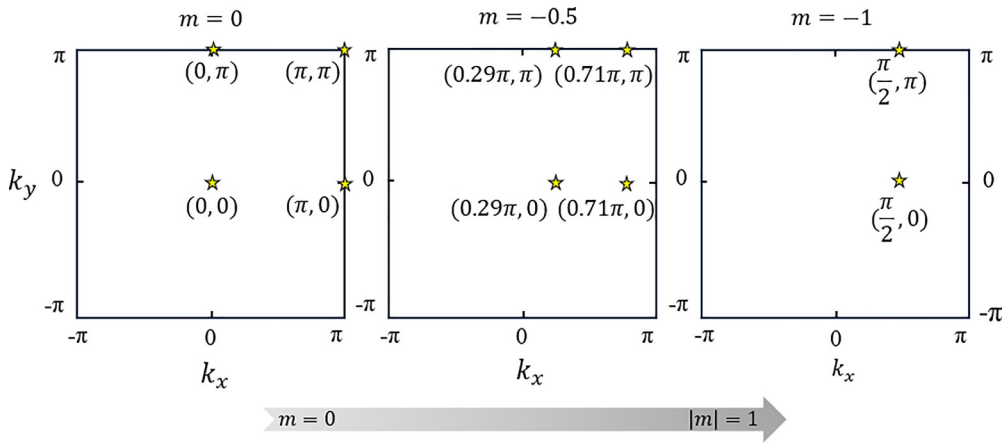

FIG. 7. The movement of EPs with changing the perturbation term.

APPENDIX E: PHOTOGRAPH IMAGE OF FABRICATED CIRCUIT SAMPLE WITH THE 6_3^3 LINK EP

As shown in Fig. 8, we plot the photograph image of the fabricated circuit sample with the 6_3^3 link EP.

APPENDIX F: DETAILS OF THE METHOD OF CIRCUIT FABRICATION

We fabricate electronic circuits using LCEDA program software, where PCB stacking, internal layers, and the wiring method are properly designed. Here, sample PCBs have six-layer board structure, where the top and bottom layers are used to wire and place components. The two nonadjacent inner layers are used as the power supply layers for active devices and the remaining two inner layers are grounding layers, which not only synchronizes the power supply, but also facilitate heat dissipation. Furthermore, we made the wiring as short as possible while also selecting a relatively large width (0.6 mm) to minimize parasitic effects. Using the multilayer design of circuit PCBs, we note that electric circuits provide a useful platform for exploring the complicated knot topology of EPs. It is worth noting that the filtering capacitors are placed at each active device supply pin, which can filter ac noise and high-frequency interference signals to provide a stable dc operating voltage for the multipliers (0.01 μf) and amplifiers (0.1 and 2.2 μf). The amplifier driving the capacitive load introduces a resistor ($R_0 = 5\ \Omega$) close to the OpAmp to ensure output stability. The pins or SMP connectors are soldered to both the PCB nodes and the multiplier inputs for external voltage input. To ensure high accuracy and low losses of the circuit components (the disorder strength is only 1%), we use a WK6500B impedance analyzer to select circuit elements.

APPENDIX G: SIMULATION RESULTS OF IMPEDANCE SPECTRA

As shown in Figs. 9(a)–9(c), we plot the simulation impedance spectra of node 1 with the external voltages being ($V_a = V_b = -5$ V), ($V_a = -V_b = -5$ V), and ($V_a = -V_b = 5$ V) of the circuit sample with a trefoil knot EP_2, a 6_3^3 link EP_3 and a sixth-order EP.

APPENDIX H: DETAILS OF THE EXPERIMENTAL MEASUREMENTS

In order to efficiently excite circuits containing adjustable nonreciprocal coupling and constant nonreciprocal coupling, we set the ac input signal at the circuit nodes. At the same time, we choose ±15 V dc voltage source to supply the active device and vary external voltages of the multipliers to achieve tunable couplings by adjusting the dc voltage source amplitude. The measured impedance spectra and impedance profiles possess the same form when the external input voltage takes different values.

Furthermore, to recover the circuit Laplacian eigenspectra, the voltage response of all circuit nodes should be measured by the oscilloscope when an ac voltage with the form of $V_0 e^{i\omega t}$ ($\omega = 2\pi f$) is applied to the circuit nodes. Then we motivate all circuit nodes to repeat the process. The voltage source is connected in series with a precision resistor to the PCB. Here, $V_i(j)$ corresponds to the measured voltage at node i under the voltage excitation at node j with I_j. The ac voltage source current I_j is calculated by Ohm's law $I = U/R$, where U is the voltage difference across the precision resistor obtained from the oscilloscope, and R is the resistance of the precision resistor. Based on the measured voltages and exciting currents, we can get the inverse of circuit Laplacian G [$G_{ij} = V_i(j)/I_j$], after which the circuit Laplacian J can

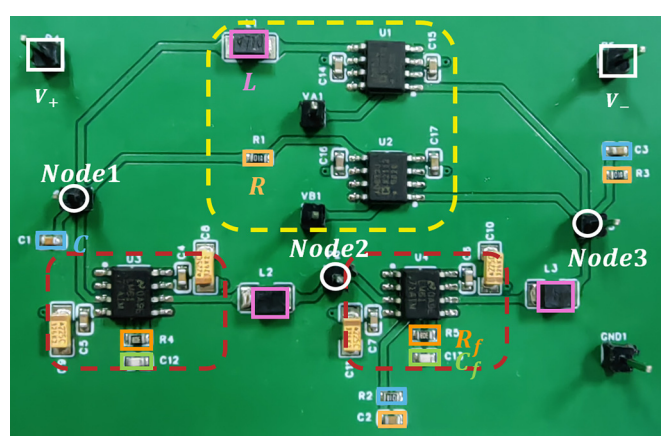

FIG. 8. The photograph image of a fabricated circuit sample with the 6_3^3 link EP.

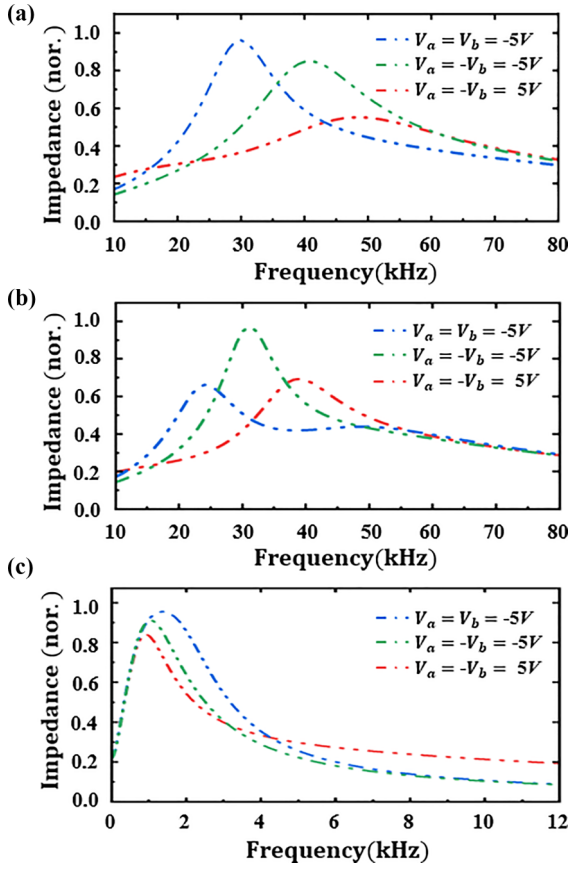

FIG. 9. The simulation results of impedance spectra. (a)–(c) The simulation impedance spectra of node 1 with the external voltages being ($V_a = V_b = -5$ V), ($V_a = -V_b = -5$ V), and ($V_a = -V_b = 5$ V) of the circuit sample with a trefoil knot EP_2, a 6_3^3 link EP_3, and a sixth-order EP.

be recovered from $J = G^{-1}$. Based on the recovered circuit Laplacian, the non-Hermitian Hamiltonian of a pth-order EP related to a (p, q)-torus knot can be written as $H_{(p,q)} = i\omega L J_{(p,q)} + \frac{i\omega L}{R} I_p$ with I_p being a pth-order identity matrix (see Appendix D for details). Similarly, the non-Hermitian Hamiltonian of a two-generation nested-link EP can be written as $H_N = \frac{1}{i\omega C} J + (1 + \frac{1}{\omega^2 L_g C} - \frac{1}{\omega C R_g}) I_N$ with I_N being a pth-order identity matrix (see Appendix K for details). In this case, we can get the recovered circuit Laplacian eigenspectra.

APPENDIX I: NUMERICAL CALCULATIONS AND EXPERIMENTAL MEASUREMENTS ON THE SPLITTING BEHAVIORS OF EIGENSPECTRA PASSING THROUGH THE EPs

In this appendix, we conducted theoretical calculations (solid lines) and experimental measurements (discrete points) on the splitting behavior of real and imaginary parts of eigenspectra passing through the trefoil knot EP_2 along the $k_y = 0$ path, as shown in Figs. 10(a) and 10(b). It can be observed that the trefoil knot EP_2 exhibits a nonlinear splitting *in the form of* $E \sim |k|^{3/2}$, but the knot structure near this EP_2 cannot be discerned. Furthermore, the splitting behaviors along the $k_y = 0$ path for the EP_3 with 6_3^3 link topology and the EP_6 with nested-link topology *in the form of* $E \sim |k|$ are presented in Figs. 10(c) and 10(d) and Figs. 10(e) and 10(f), respectively. We can see that both the real and imaginary parts of energy spectra display the linear dispersion near these EPs, manifesting the dispersion behavior of Dirac EPs.

APPENDIX J: NUMERICAL RESULTS OF EIGENSPECTRA WITH DIFFERENT NESTED-LINK TOPOLOGIES AROUND EPs

In this appendix, we present numerical results of eigenspectra with different nested-link/knot topologies around EPs. Figures 11(a) and 11(b) plot the eigenspectra and evolution of eigenenergies around EPs with different nested-link topologies with ($n_1 = 4$, $n_2 = 2$), ($n_1 = 2$, $n_2 = 2$, $n_3 = 2$), respectively. It is clearly shown that higher-order Dirac EPs with different nested-link topologies appear at the origin of 2D k space.

APPENDIX K: DETAILED DERIVATION OF CIRCUIT LAPLACIAN SUSTAINING EPs WITH THE TWO-GENERATION NESTED-LINK TOPOLOGIES

Applying Kirchhoff's law to the six circuit nodes for the sixth-order exceptional point circuit, we get the following equations as

$$I_1 = I_{L_g} + \sum_{n=1}^{6} (I_{C_{a,n}} + I_{R_{b,n}}), \tag{K1a}$$

$$I_2 = I_{R_g} + i\omega C(V_1 - V_2), \tag{K1b}$$

$$I_3 = I_{R_g} + i\omega C(V_2 - V_3), \tag{K1c}$$

$$I_4 = I_{R_g} + i\omega C(V_3 - V_4), \tag{K1d}$$

$$I_5 = I_{R_g} + i\omega C(V_4 - V_5), \tag{K1e}$$

$$I_6 = I_{R_g} + i\omega C(V_5 - V_6). \tag{K1f}$$

The current Kirchhoff equation for node c is $I_C = \frac{V_1 - V_C}{R_{01}} + \frac{0 - V_C}{R_{11}}$. This node has no current output to the external environment and therefore $I_C = 0$. It can be derived that $V_C = cV_1$ with $c = \frac{R_{01}}{R_{11} + R_{01}}$. Using the transfer function of the multipliers, we can obtain the detailed expression of Eq. (K1) as

$$\begin{aligned} I_1 = {} & \left(\frac{V_{a,1}V_C}{10} - V_1\right) i\omega C_{a,1} + \left(\frac{V_{b,1}V_C}{10} - V_1\right)\frac{1}{R_{b,1}} \\ & + \left(\frac{V_{a,2}V_2}{10} - V_1\right) i\omega C_{a,2} + \left(\frac{V_{b,2}V_2}{10} - V_1\right)\frac{1}{R_{b,2}} \\ & + \left(\frac{V_{a,3}V_3}{10} - V_1\right) i\omega C_{a,3} + \left(\frac{V_{b,3}V_3}{10} - V_1\right)\frac{1}{R_{b,3}} \\ & + \left(\frac{V_{a,4}V_4}{10} - V_1\right) i\omega C_{a,4} + \left(\frac{V_{b,4}V_4}{10} - V_1\right)\frac{1}{R_{b,4}} \\ & + \left(\frac{V_{a,5}V_5}{10} - V_1\right) i\omega C_{a,5} + \left(\frac{V_{b,5}V_5}{10} - V_1\right)\frac{1}{R_{b,5}} \\ & + \left(\frac{V_{a,6}V_6}{10} - V_1\right) i\omega C_{a,6} + \left(\frac{V_{b,6}V_6}{10} - V_1\right)\frac{1}{R_{b,6}} - \frac{V_1}{i\omega L_g}, \end{aligned} \tag{K2a}$$

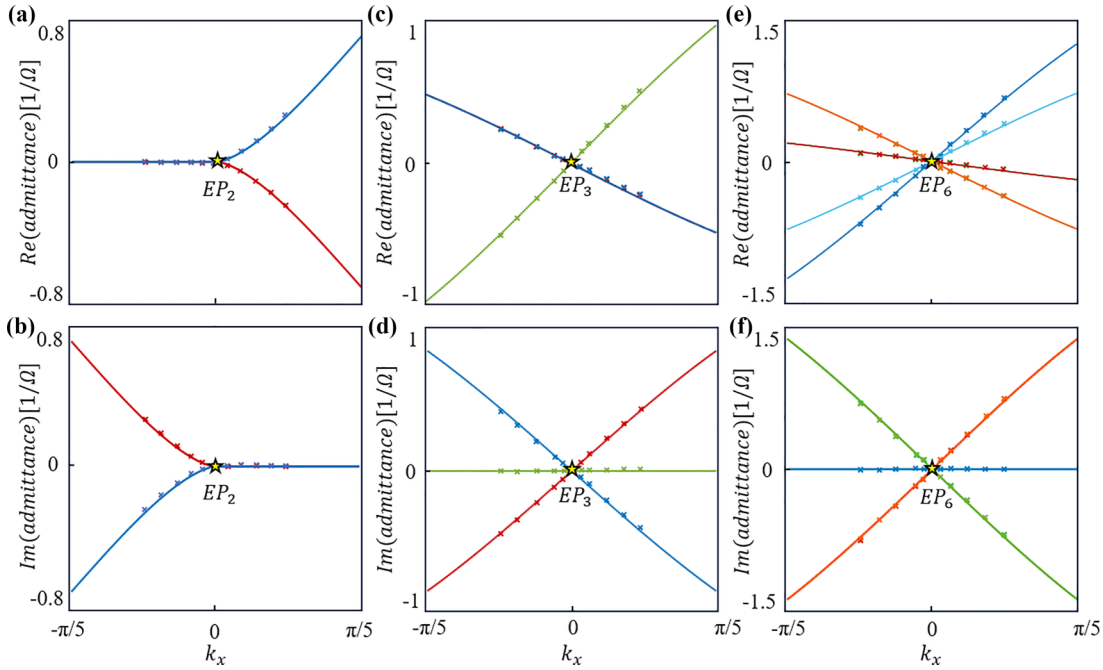

FIG. 10. The splitting behavior passing through the EPs. (a), (b) The real and imaginary parts of eigenspectra of the trefoil knot EP_2. (c), (d) The real and imaginary parts of eigenspectra of EP_3 with the 6_3^3 link topology. (e), (f) The real and imaginary parts of eigenspectra of EP_6 with the nested-link topology.

$$I_2 = i\omega C(V_1 - V_2) - \frac{V_2}{R_g}, \tag{K2b}$$

$$I_3 = i\omega C(V_2 - V_3) - \frac{V_3}{R_g}, \tag{K2c}$$

$$I_4 = i\omega C(V_3 - V_4) - \frac{V_4}{R_g}, \tag{K2d}$$

$$I_5 = i\omega C(V_4 - V_5) - \frac{V_5}{R_g}, \tag{K2e}$$

$$I_6 = i\omega C(V_5 - V_6) - \frac{V_6}{R_g}, \tag{K2f}$$

with $V_{a,1} = \frac{100a_1}{c}$, $V_{b,1} = \frac{100b_1}{c}$; $V_{a,3} = 10a_3$, $V_{b,3} = 10b_3$; and $V_{a,n} = 100a_n$, $V_{b,n} = 100b_n$ $(n = 2, 4, 5, 6)$. It is noted that due to the different order of magnitude of the Hamiltonian elements, we design the corresponding load capacitors and resistors for the multiplier module so that when the circuit Laplacian matrix matches the Hamiltonian elements, the external input voltage required for the multiplier falls within the effective voltage range. Meanwhile, the resistors and capacitors in each multiplier module have to satisfy $R_{b,n} = \frac{1}{\omega C_{a,n}}$ $(n = 1, \ldots, 6)$. Choosing $C_{a,n} = 0.1C$, $R_{b,n} = \frac{1}{\omega C_{a,n}} = \frac{10}{\omega C}$ $(n = 1, 2, 4, 5, 6)$, $C_{a,3} = C$, and $R_{b,3} = \frac{1}{\omega C}$, Eq. (K2) can be written in the matrix form as

$$\begin{pmatrix} I_1 \\ I_2 \\ I_3 \\ I_4 \\ I_5 \\ I_6 \end{pmatrix} = i\omega C \begin{pmatrix} G_1 - \left(1.5 - \frac{1}{\omega^2 C L_g} - 1.5i\right) & G_2 & G_3 & G_4 & G_5 & G_6 \\ 1 & D & 0 & 0 & 0 & 0 \\ 0 & 1 & D & 0 & 0 & 0 \\ 0 & 0 & 1 & D & 0 & 0 \\ 0 & 0 & 0 & 1 & D & 0 \\ 0 & 0 & 0 & 0 & 1 & D \end{pmatrix} \begin{pmatrix} V_1 \\ V_2 \\ V_3 \\ V_4 \\ V_5 \\ V_6 \end{pmatrix}, \tag{K3}$$

with $G_n = a_n - ib_n$ $(n = 1, \ldots, 6)$, $D = -(1 + \frac{1}{\omega^2 L_g C} - \frac{1}{\omega C R_g}) = -1 + 1.5i$, and the parameters are set as $R_g = \frac{2}{3\omega C}$ and $L_g = \frac{2}{\omega^2 C}$ to complete the constants of the diagonal elements. The remaining constant part on the diagonal only induces a constant shift and the eigenspectra structure is not affected. We note that Eq. (K3) possesses the same form with the Hamiltonian matrix of H_6, where the k-dependent effective tight-binding parameters $t_j(\boldsymbol{k_x}, \boldsymbol{k_y})$ can be realized by tuning external voltages of $V_{a,n}$ and $V_{b,n}$ to make the equation $a_n - b_n i = t_{n-1}(\boldsymbol{k_x}, \boldsymbol{k_y})$ satisfied at different k vectors.

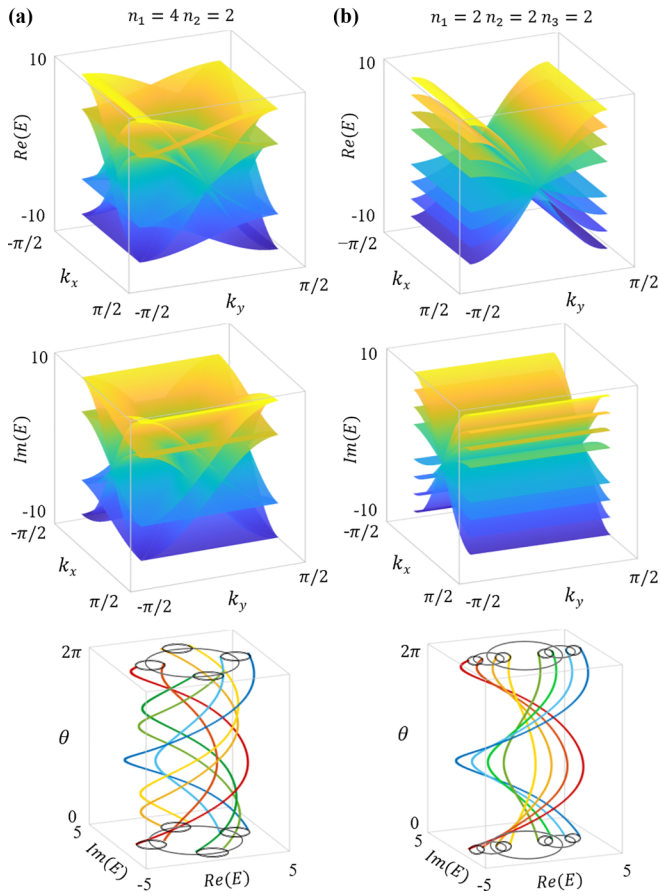

FIG. 11. Numerical results of eigenspectra with different knot and link topologies around EPs. (a), (b) The eigenspectra and evolution of eigenenergies around EPs with different nested-link topologies with ($n_1 = 4, n_2 = 2$), ($n_1 = 2, n_2 = 2, n_3 = 2$).

APPENDIX L: NUMERICAL RESULTS ON THE REAL AND IMAGINARY PARTS OF EIGENSPECTRA ALONG DIFFERENT PATHS

The dispersion cuts along three paths of $k_x = k_y$, $k_x = 0$, and $2k_x = k_y$ for three EPs considered in our work are shown in Figs. 12(a), 12(c), and 12(e) for the real part of eigenspectra, and Figs. 12(b), 12(d), and 12(f) for the imaginary part of eigenspectra. It can be observed that the trefoil knot EP_2 exhibits a nonlinear splitting. Furthermore, both the real and imaginary parts of energy spectra display the linear dispersion near Dirac EPs.

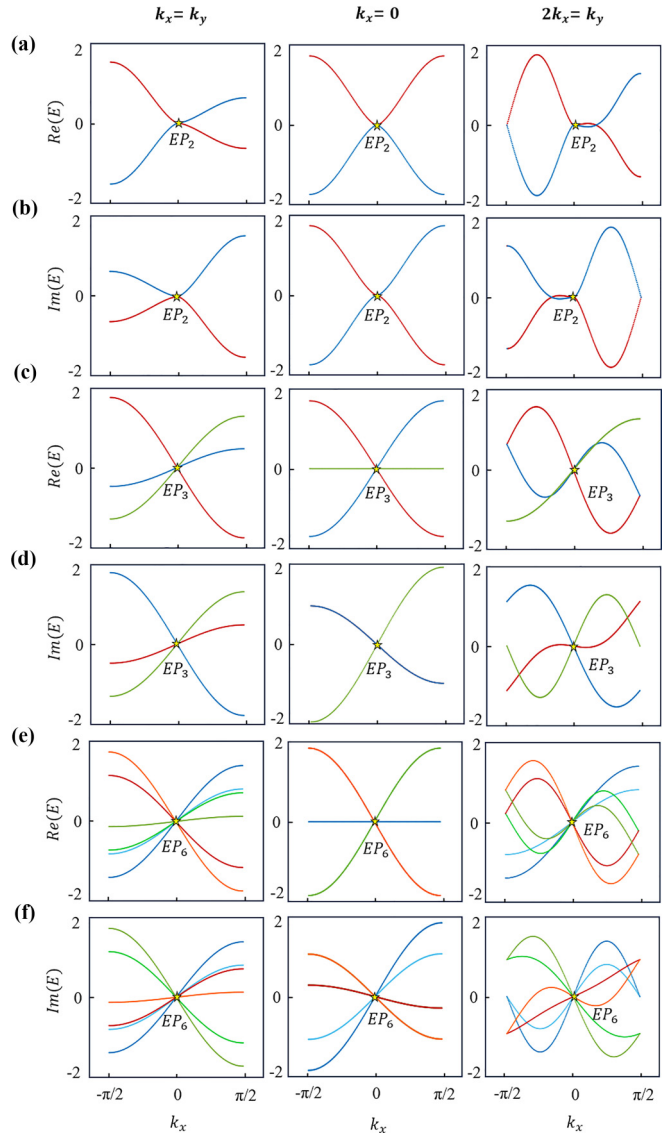

FIG. 12. (a), (c), (e) and (b), (d), (f) The real and imaginary parts of eigenspectra along three paths of $k_x = k_y$, $2k_x = k_y$, and $k_x = 0$ through trefoil knot EP_2, 6_3^3 link EP_3, and EP_6 with the nested link.

[1] N. Moiseyev, *Non-Hermitian Quantum Mechanics* (Cambridge University Press, Cambridge, UK, 2011).

[2] R. El-Ganainy, K. G. Makris, M. Khajavikhan, Z. H. Musslimani, S. Rotter, and D. N. Christodoulides, Non-Hermitian physics and PT symmetry, Nat. Phys. **14**, 11 (2018).

[3] Y. Ashida, Z. Gong, and M. Ueda, Non-Hermitian physics, Adv. Phys. **69**, 249 (2020).

[4] E. J. Bergholtz, J. C. Budich, and F. K. Kunst, Exceptional topology of non-Hermitian systems, Rev. Mod. Phys. **93**, 015005 (2021).

[5] T. Kato, *Perturbation Theory for Linear Operators, Classics in Mathematics* (Springer Science & Business Media, Berlin, 2013) Vol. 132.

[6] L. Zin, H. Ramezani, T. Eichelkraut, T. Kottos, H. Cao, and D. N. Christodoulides, Unidirectional invisibility induced by $\mathcal{PT}$-symmetric periodic structures, Phys. Rev. Lett. **106**, 213901 (2011).

[7] L. Feng, Y. Xu, W. S. Fegadolli, M. Lu, J. E. B. Oliveira, V. R. Almeida, Y. Chen, and A. Scherer, Experimental demonstration of a unidirectional reflectionless parity-time metamaterial at optical frequencies, Nat. Mater. **12**, 108 (2013).

[8] W. Chen, S. K. Özdemir, G. Zhao, J. Wiersig, and L. Yang, Exceptional points enhance sensing in an optical microcavity, Nature (London) **548**, 192 (2017).

[9] H. Hodaei, A. U. Hassan, S. Wittek, H. Garcia-Gracia, R. El-Ganainy, D. N. Christodoulides, and M. Khajavikhan, Enhanced sensitivity at higher-order exceptional points, Nature (London) **548**, 187 (2017).

[10] L. Feng, Z. Wong, R. Ma, Y. Wang, and X. Zhang, Single-mode laser by parity-time symmetry breaking, Science **346**, 972 (2014).

[11] M. A. Miri and A. Alu, Exceptional points in optics and photonics, Science **363**, eaar7709 (2019).

[12] W. D. Heiss, The physics of exceptional points, J. Phys. A: Math. Theor. **45**, 444016 (2012).

[13] Ş. K. Özdemir, S. Rotter, F. Nori, and L. Yang, Parity–time symmetry and exceptional points in photonics, Nat. Mater. **18**, 783 (2019).

[14] B. Zhen, C. W. Hsu, Y. Igarashi, L. Lu, I. Kaminer, A. Pick, S. L. Chua, J. D. Joannopoulos, and M. Soljačić, Spawning rings of exceptional points out of Dirac cones, Nature (London) **525**, 354 (2015).

[15] T. Wu, W. Zhang, H. Zhang, S. Hou, G. Chen, R. Liu, C. Lu, J. Li, R. Wang, P. Duan, J. Li, B. Wang, L. Shi, J. Zi, and X. Zhang, Vector exceptional points with strong superchiral fields, Phys. Rev. Lett. **124**, 083901 (2020).

[16] B. Peng, Ş. K. Özdemir, S. Rotter, H. Yilmaz, M. Liertzer, F. Monifi, C. M. Bender, F. Nori, and L. Yang, Loss-induced suppression and revival of lasing, Science **346**, 328 (2014).

[17] P. Miao, Z. Zhang, J. Sun, W. Walasik, S. Longhi, N. M. Litchinitser, and L. Feng, Orbital angular momentum microlaser, Science **353**, 464 (2016).

[18] L. Feng, R. El-Ganainy, and L. Ge, Non-Hermitian photonics based on parity–time symmetry, Nat. Photon **11**, 752 (2017).

[19] K. Ding, G. Ma, M. Xiao, Z. Zhang, and C. Chan, Emergence, coalescence, and topological properties of multiple exceptional points and their experimental realization, Phys. Rev. X **6**, 021007 (2016).

[20] J. H. Park, A. Ndao, W. Cai, L. Hsu, A. Kodigala, T. Lepetit, Y. H. Lo, and B. Kanté, Symmetry-breaking-induced plasmonic exceptional points and nanoscale sensing, Nat. Phys. **16**, 462 (2020).

[21] J. C. Budich, J. Carlström, F. K. Kunst, and E. J. Bergholtz, Symmetry-protected nodal phases in non-Hermitian systems, Phys. Rev. B **99**, 041406(R) (2019).

[22] S. Sayyad and F. K. Kunst, Realizing exceptional points of any order in the presence of symmetry, Phys. Rev. Res. **4**, 023130 (2022).

[23] P. Delplace, T. Yoshida, and Y. Hatsugai, Symmetry-protected multifold exceptional points and their topological characterization, Phys. Rev. Lett. **127**, 186602 (2021).

[24] M. Stålhammar and E. J. Bergholtz, Classification of exceptional nodal topologies protected by $\mathcal{PT}$ symmetry, Phys. Rev. B **104**, L201104 (2021).

[25] H. Zhou, C. Peng, Y. Yoon, C. W. Hsu, K. A. Nelson, L. Fu, J. D. Joannopoulos, M. Soljačić, and B. Zhen, Observation of bulk Fermi arc and polarization half charge from paired exceptional points, Science **359**, 1009 (2018).

[26] Y. Xiao, J. Hu, Z. Zhang, and C. T. Chan, Experimental demonstration of splitting rules for exceptional points and their topological characterization, Phys. Rev. B **108**, 115427 (2023).

[27] Z. Li, G. Cardoso, E. J. Bergholtz, and Q. Jiang, Braids and higher-order exceptional points from the interplay between lossy defects and topological boundary states, arXiv:2312.03054.

[28] C. Dembowski, H. D. Gräf, H. L. Harney, A. Heine, W. D. Heiss, H. Rehfeld, and A. Richter, Experimental observation of the topological structure of exceptional points, Phys. Rev. Lett. **86**, 787 (2001).

[29] I. Gilary, A. A. Mailybaev, and N. Moiseyev, Time-asymmetric quantum-state-exchange mechanism, Phys. Rev. A **88**, 010102(R) (2013).

[30] A. U. Hassan, B. Zhen, M. Soljačić, M. Khajavikhan, and D. N. Christodoulides, Dynamically encircling exceptional points: Exact evolution and polarization state conversion, Phys. Rev. Lett. **118**, 093002 (2017).

[31] X. Zhang, S. Wang, B. Hou, and C. Chan, Dynamically encircling exceptional points: *In situ* control of encircling loops and the role of the starting point, Phys. Rev. X **8**, 021066 (2018).

[32] J. W. Yoon, Y. Choi, C. Hahn, G. Kim, S. H. Song, K. Y. Yang, J. Y. Lee, Y. Kim, C. S. Lee, J. K. Shin, and H. S. Lee, Time-asymmetric loop around an exceptional point over the full optical communications band, Nature (London) **562**, 86 (2018).

[33] H. Nasari, G. Lopez-Galmiche, H. E. Lopez-Aviles, A. Schumer, A. U. Hassan, Q. Zhong, S. Rotter, P. LiKamWa, D. N. Christodoulides, and M. Khajavikhan, Observation of chiral state transfer without encircling an exceptional point, Nature (London) **605**, 256 (2022).

[34] J. Doppler, A. A. Mailybaev, J. Böhm, U. Kuhl, A. Girschik, F. Libisch, T. J. Milburn, P. Rabl, N. Moiseyev, and S. Rotter, Dynamically encircling an exceptional point for asymmetric mode switching, Nature (London) **537**, 76 (2016).

[35] H. Xu, D. Mason, L. Jiang, and J. G. E. Harris, Topological energy transfer in an optomechanical system with exceptional points, Nature (London) **537**, 80 (2016).

[36] H. Shen, B. Zhen, and L. Fu, Topological band theory for non-Hermitian Hamiltonians, Phys. Rev. Lett. **120**, 146402 (2018).

[37] Z. Yang, A. P. Schnyder, J. Hu, and C. K. Chiu, Fermion doubling theorems in two-dimensional non-Hermitian systems for Fermi points and exceptional points, Phys. Rev. Lett. **126**, 086401 (2021).

[38] K. Ding, C. Fang, and G. Ma, Non-Hermitian topology and exceptional-point geometries, Nat. Rev. Phys. **4**, 745 (2022).

[39] C. C. Wojcik, X. Sun, T. Bzdušek, and S. Fan, Homotopy characterization of non-Hermitian Hamiltonians, Phys. Rev. B **101**, 205417 (2020).

[40] L. Zhi and R. S. Mong, Homotopical characterization of non-Hermitian band structures, Phys. Rev. B **103**, 155129 (2021).

[41] W. Tang, X. Jiang, K. Ding, Y. Xiao, Z. Q. Zhang, C. Chan, and G. Ma, Exceptional nexus with a hybrid topological invariant, Science **370**, 1077 (2020).

[42] H. Hu and E. Zhao, Knots and non-Hermitian Bloch bands, Phys. Rev. Lett. **126**, 010401 (2021).

[43] K. Wang, A. Dutt, C. C. Wojcik, and S. Fan, Topological complex-energy braiding of non-Hermitian bands, Nature (London) **598**, 59 (2021).

[44] Y. S. S. Patil, J. Holler, P. A. Henry, C. Guria, Y. Zhang, L. Jiang, N. Kralj, N. Read, and J. G. E. Harris, Measuring the knot of non-Hermitian degeneracies and non-commuting braids, Nature (London) **607**, 271 (2022).

[45] Q. Zhang, Y. Li, H. Sun, X. Liu, L. Zhao, X. Feng, X. Fan, and C. Qiu, Observation of acoustic non-Hermitian Bloch braids and associated topological phase transitions, Phys. Rev. Lett. **130**, 017201 (2023).

[46] K. Yang, Z. Li, J. L. K. König, L. Rødland, M. Stålhammar, and E. J. Bergholtz, Homotopy, symmetry, and non-Hermitian band topology, arXiv:2309.14416.

[47] H. Hu, S. Sun, and S. Chen, Knot topology of exceptional point, and non-Hermitian no-go theorem, Phys. Rev. Res. **4**, L022064 (2022).

[48] J. H. D. Rivero, L. Feng, and L. Ge, Imaginary gauge transformation in momentum space and Dirac exceptional point, Phys. Rev. Lett. **129**, 243901 (2022).

[49] C. C. Wojcik, K. Wang, A. Dutt, J. Zhong, and S. Fan, Eigenvalue topology of non-Hermitian band structures in two and three dimensions, Phys. Rev. B **106**, L161401 (2022).

[50] J. Ningyuan, C. Owens, A. Sommer, D. Schuster, and J. Simon, Time-and site-resolved dynamics in a topological circuit, Phys. Rev. X **5**, 021031 (2015).

[51] V. V. Albert, L. I. Glazman, and L. Jiang, Topological properties of linear circuit lattices, Phys. Rev. Lett. **114**, 173902 (2015).

[52] C. H. Lee, S. Imhof, C. Berger, F. Bayer, J. Brehm, L. W. Molenkamp, T. Kiessling, and R. Thomale, Topolectrical circuits, Commun. Phys. **1**, 39 (2018).

[53] S. Imhof, C. Berger, F. Bayer, J. Brehm, L. W. Molenkamp, T. Kiessling, F. Schindler, C. H. Lee, M. Greiter, T. Neupert, and R. Thomale, Topolectrical-circuit realization of topological corner modes, Nat. Phys. **14**, 925 (2018).

[54] Y. Hadad, J. C. Soric, A. B. Khanikaev, and A. Alu, Self-induced topological protection in nonlinear circuit arrays, Nat. Electron. **1**, 178 (2018).

[55] F. Zangeneh-Nejad and R. Fleury, Nonlinear second-order topological insulators, Phys. Rev. Lett. **123**, 053902 (2019).

[56] M. Ezawa, Electric circuit simulations of nth-Chern-number insulators in $2n$-dimensional space and their non-Hermitian generalizations for arbitrary n, Phys. Rev. B **100**, 075423 (2019).

[57] Y. Wang, H. M. Price, B. Zhang, and Y. D. Chong, Circuit implementation of a four-dimensional topological insulator, Nat. Commun. **11**, 2356 (2020).

[58] N. A. Olekhno, E. I. Kretov, A. A. Stepanenko, P. A. Ivanova, V. V. Yaroshenko, E. M. Puhtina, D. S. Filonov, B. Cappello, L. Matekovits, and M. A. Gorlach, Topological edge states of interacting photon pairs emulated in a topolectrical circuit, Nat. Commun. **11**, 1436 (2020).

[59] T. Helbig, T. Hofmann, S. Imhof, M. Abdelghany, T. Kiessling, L. W. Molenkamp, C. H. Lee, A. Szameit, M. Greiter, and R. Thomale, Generalized bulk–boundary correspondence in non-Hermitian topolectrical circuits, Nat. Phys. **16**, 747 (2020).

[60] W. Zhang, D. Zou, Q. Pei, W. He, J. Bao, H. Sun, and X. Zhang, Experimental observation of higher-order topological Anderson insulators, Phys. Rev. Lett. **126**, 146802 (2021).

[61] A. Stegmaier, S. Imhof, T. Helbig, T. Hofmann, C. H. Lee, M. Kremer, A. Fritzsche, T. Feichtner, S. Klembt, S. Höfling, and I. Boettcher, Topological defect engineering and $\mathcal{PT}$ symmetry in non-Hermitian electrical circuits, Phys. Rev. Lett. **126**, 215302 (2021).

[62] S. Liu, R. Shao, S. Ma, L. Zhang, O. You, H. Wu, Y. Xiang, T. Cui, and S. Zhang, Non-Hermitian skin effect in a non-Hermitian electrical circuit, Research **2021**, 5608038 (2021).

[63] B. Lv, R. Chen, R. Li, C. Guan, B. Zhou, G. Dong, C. Zhao, Y. Li, Y. Wang, H. Tao, and J. Shi, Realization of quasicrystalline quadrupole topological insulators in electrical circuits, Commun. Phys. **4**, 126 (2021).

[64] R. Li, B. Lv, H. Tao, J. Shi, Y. Chong, B. Zhang, and H. Chen, Ideal type-II Weyl points in topological circuits, Natl. Sci. Rev. **8**, nwaa192 (2021).

[65] W. Zhang, H. Yuan, N. Sun, H. Sun, and X. Zhang, Observation of novel topological states in hyperbolic lattices, Nat. Commun. **13**, 2937 (2022).

[66] M. Di Ventra, Y. V. Pershin, and C. C. Chien, Custodial chiral symmetry in a Su-Schrieffer-Heeger electrical circuit with memory, Phys. Rev. Lett. **128**, 097701 (2022).

[67] L. Song, H. Yang, Y. Cao, and P. Yan, Square-root higher-order Weyl semimetals, Nat. Commun. **13**, 5601 (2022).

[68] P. M. Lenggenhager, A. Stegmaier, L. K. Upreti, T. Hofmann, T. Helbig, A. Vollhardt, M. Greiter, C. H. Lee, S. Imhof, H. Brand, and T. Kießling, Simulating hyperbolic space on a circuit board, Nat. Commun. **13**, 4373 (2022).

[69] P. Zhu, X. Sun, T. L. Hughes, and G. Bahl, Higher rank chirality and non-Hermitian skin effect in a topolectrical circuit, Nat. Commun. **14**, 720 (2023).

[70] W. Zhang, H. Wang, H. Sun, and X. Zhang, Non-Abelian inverse Anderson transitions, Phys. Rev. Lett. **130**, 206401 (2023).

[71] S. S. Yamada, T. Li, M. Lin, C. W. Peterson, T. L. Hughes, and G. Bahl, Bound states at partial dislocation defects in multipole higher-order topological insulators, Nat. Commun. **13**, 2035 (2022).

[72] D. Rolfsen, *Knots and Links* (American Mathematical Society, Providence, RI, 2003).

[73] L. Kong, W. Zhang, P. Li, X. Guo, J. Zhang, F. Zhang, J. Zhao, and X. Zhang, High capacity topological coding based on nested vortex knots and links, Nat. Commun. **13**, 2705 (2022).